Numerical analysis of penetration, radiation, and scattering for a 2D slotted semielliptical channel filled with isorefractive material

Danilo Erricolo(*), Michael D. Lockard(**),

Chalmers M. Butler(**), Piergiorgio L. E. Uslenghi(*)

(*)Department of Electrical and Computer Engineering

University of Illinois at Chicago

851 South Morgan St

Chicago, IL 60607

(**)Holcombe Department of Electrical and Computer Engineering

Clemson University,

Clemson, SC 29634USA

Short title: Numerical analysis for a 2D semielliptical channel

Corresponding author:

Danilo Erricolo

Department of Electrical and Computer Engineering

University of Illinois at Chicago

851 South Morgan St

Chicago, IL 60607 email: derricol@ece.uic.edu

phone:(312) 996 5771, fax: (312) 996 6465

Abstract

Electromagnetic penetration through an aperture into a cavity is considered. The structure of interest comprises a slotted infinite conducting plane backed by a semielliptical channel. Three independent integral equations are used to study the structure of interest, for which analytical expressions are derived in another paper and involve summations of Mathieu functions. Numerical results from the analytical expressions for the electromagnetic fields are compared with those from integral equation methods for various cases of excitation and isorefractive materials. The agreement is excellent in all cases.

1 Introduction

Two different methods are considered to determine the electromagnetic field in the structure whose cross-section is illustrated in Fig. 1. The structure consists of a slotted metallic plane backed by a semielliptical cavity with conducting walls. The media in the cavity and above the ground plane are isorefractive and the excitation may be a $z-$independent plane wave or line source in the exterior region or a $z-$independent line source in the interior region. The harmonic time variation e^{jwt} is suppressed for all expressions presented. Analytic expressions for the electromagnetic field in the cavity and outside the ground plane were found in [1]. Because an exact analytical solution for the field can be determined in terms of tabulated functions, one may look upon this problem as canonical, yet it is by no means simple. In fact, the structure comprises a cavity, sharp edges, and two isorefractive media, which prompts one to expect a field with varied features.

One goal of this work is to obtain two independent solutions for the electromagnetic field in the structure of Fig. 1. Data found by evaluating the analytic expressions of [1] are compared with those obtained from numerical solutions of three sets of independent integral equations. The work presented here was originally initiated to tabulate the analytic solutions of [1] in order to establish a benchmark for the validation of the integral equation results. As the authors pursued this goal, the computation of the analytic solutions proved to be quite involved due to the need to evaluate Mathieu functions over a wide range of parameters and to sum slowly convergent infinite series of these functions. Consequently, the objectives evolved to

the point that the primary goal of the project has become a mutual validation of independent solution methods.

The major contributions of this paper are twofold. On one hand, for the first time, numerical results are recorded for the canonical problem of field penetration through the channel-backed slot of Fig. 1. On the other hand, three specific integral equation methods are developed to investigate the field present near the structure of Fig. 1 and to validate the numerical results obtained from evaluating the expressions of [1]. However, one must bear in mind that the integral equation methods are applicable to more general structures, such as the one of Fig. 3.

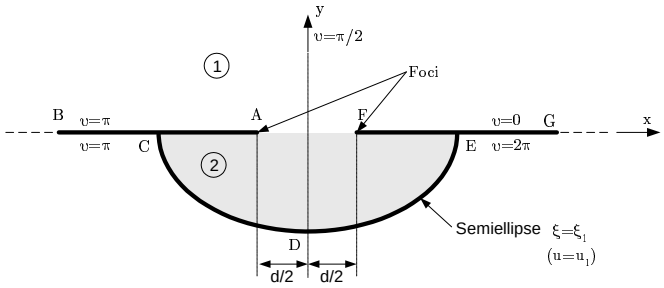

Figure 1: Semielliptical Channel-Backed Slot.

This paper is organized as follows. The geometry of the structure is described in detail. Appropriate integral equations are formulated and techniques for solving them numerically are suggested. The comparisons among the numerical values of the analytical solution and those obtained from the integral equations are discussed. The behavior of the electromagnetic fields inside and outside the cavity is examined for different excitations: plane wave, line source outside the cavity, and line source inside the cavity. Two polarizations are considered for each source excitation case. Results

are provided for different values of the ratio of the impedances of the two isorefractive materials and also for different values of the ratio between the aperture width and the wavelength of the incident radiation. It is also verified that reciprocity is upheld. The agreement among the numerical results for the field determined by the different methods is excellent in all cases considered.

2 Geometry of structure

The structure of interest, shown in Fig. 1 in cross-section, is invariant along the z direction and is symmetric with respect to the plane $x = 0$. The slot-backing channel is a conducting cylinder of semielliptical cross-section with foci at A and F and separated by the focal distance d. The portions FG and AB of the structure are metallic half-planes each extending from a focal line to infinity. The medium in the region $y > 0$ is characterized by permittivity ε_1 and permeability μ_1; the medium inside the channel ($y < 0$ and bounded by the semiellipse CDE) has permittivity ε_2 and permeability μ_2. The two media satisfy the isorefractive condition

$$\varepsilon_1 \mu_1 = \varepsilon_2 \mu_2 \tag{1}$$

which implies that the propagation constant

$$k = \omega\sqrt{\varepsilon_1 \mu_1} = \omega\sqrt{\varepsilon_2 \mu_2} \tag{2}$$

is the same in both media. However, the intrinsic impedances are in general different:

$$Z_h = \sqrt{\frac{\mu_h}{\varepsilon_h}}, \ \ (h = 1, 2). \tag{3}$$

Because the cross-section of the channel is semielliptical (Fig. 1), it is convenient to introduce an elliptic cylinder coordinate system (u, v, z) related to the cartesian coordinate system by

$$x = \frac{d}{2} \cosh u \cos v \tag{4}$$

$$y = \frac{d}{2} \sinh u \sin v \tag{5}$$

$$z = z \tag{6}$$

where

$$0 \leq u < \infty \tag{7}$$

$$0 \leq v \leq 2\pi. \tag{8}$$

It is also convenient to introduce the variables (ξ, η, z) defined by

$$\xi = \cosh u \tag{9}$$

$$\eta = \cos v \tag{10}$$

where obviously

$$\xi \geq 1 \tag{11}$$

and

$$-1 \leq \eta \leq 1. \tag{12}$$

The coordinate surfaces with constant ξ are cylinders of elliptic cross-section with foci at A and F. Coordinate surfaces with constant η are hyperbolas with the same foci.

Observe that, if $\xi = 1$, each value of η defines a point (ξ, η) that falls on the segment of the x axis between the foci A and F. Similarly, if $\eta = 1(-1)$, each value for ξ, where $\xi > 1$, defines a point (ξ, η) on the segment of the x axis in the interval $x > d/2(x < -d/2)$. The positive portion of the y axis corresponds to $v = \pi/2$ and the negative portion, to $v = -\pi/2$. Points associated with $1 < \xi < \xi_1$ and $\pi < v < 2\pi$ fall within the semielliptical cavity.

The formulas in subsequent sections contain the dimensionless quantity

$$c = k\frac{d}{2}. \tag{13}$$

The inverse transformation from cartesian coordinates (x, y) to elliptic coordinates (ξ, η) is reported here for convenience:

$$\xi = \sqrt{\frac{4(x^2+y^2) + d^2 + \sqrt{16(x^2+y^2)^2 + d^4 - 8d^2(x^2-y^2)}}{2d^2}} \tag{14}$$

and

$$\eta = \frac{2x}{d\xi}. \tag{15}$$

3 Integral equation methods

In this section one finds an outline of integral equation methods for determining the fields in both regions of the structure in Fig. 1. Two methods are discussed for the case of a finite-width ground plane, followed by a discussion of two coupled integral equation methods which are valid for the case of an infinite ground plane. All integral equation methods presented are valid for the case of a cavity with arbitrary cross-section.

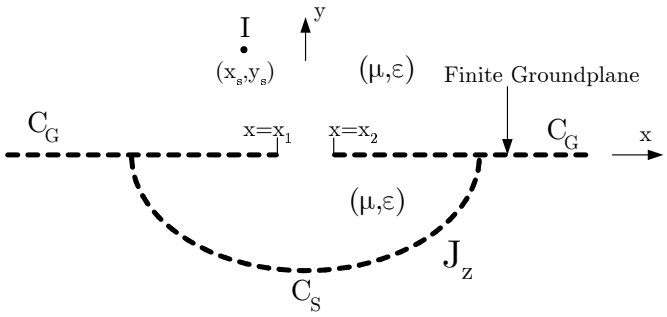

Figure 2: Geometry of structure: scatterer method ($x_1 = -\frac{d}{2}; x_2 = \frac{d}{2}$).

3.1 Finite Ground Plane Methods (TM)

Two integral equation methods are applied in the case that the ground plane is of finite width. The width of the ground plane is assumed to be so large relative to wavelength that the effects of its finite width on the field calculations are negligible. The finite ground plane methods presented are limited to cases where the source is TM-polarized and the materials in both regions are the same.

It should be noted that if the structure of interest has an infinitely wide ground plane, the approximation of a finite but large ground plane decreases accuracy for certain excitations, such as a plane wave with a low angle of incidence or a line source remote from the aperture. The effects of the finite-width ground plane are also observed when the total fields are computed in the exterior region far from the ground plane.

3.1.1 Scatterer Method

In the scatterer method the slotted plane and its channel backing is treated as a scattering body and the current induced on its conducting surfaces is determined

by integral equation methods. The finite-width ground plane, as well as the entire channel backing, is removed and an equivalent z-directed electric current is impressed on the surface $C_G \cup C_S$ formerly occupied by the conductors (Fig. 2). The tangential component of the total electric field is then forced to be zero at the location of this current, *i.e.*, on $C_G \cup C_S$ [2], resulting in

$$-\frac{k_1 Z_1}{4} \int\limits_{C_G \cup C_s} J_z(x', y') H_0^{(2)} \left(k_1 \sqrt{(x-x')^2 + (y-y')^2} \right) dl' = -E_z^i(x, y) \ , \ x, y \in C_G \cup C_s \tag{16}$$

where

$$E_z^i(x, y) = e^{jk_1(x \cos\phi_o + y \sin\phi_o)} \tag{17}$$

or

$$E_z^i(x, y) = -\frac{k_1 Z_1}{4} I H_0^{(2)} \left(k_1 \sqrt{(x-x_s)^2 + (y-y_s)^2} \right) \tag{18}$$

for plane wave excitation and excitation by a line source of strength I, respectively. The integral equation can be solved by standard numerical techniques involving discretization of surfaces, introduction of basis and testing functions, and a solution to a matrix equation for unknown weighting factors. The numerical results presented in this paper are obtained by using a rectangular pulse basis function and a Dirac delta testing function for both finite ground plane methods.

3.1.2 Schelkunoff Method

The results of the scatterer method were compared with those of the Schelkunoff method [2] to verify accuracy and also to observe the benefits of the latter method. The results of the Schelkunoff method, unlike those of the scatterer method, remain

accurate in the case in which the total field in the interior of the channel is very small compared to the incident field.

3.2 Infinite Ground Plane Methods

Coupled integral equations for the channel-backed slot problem are derived in the usual way [3]. The aperture is shorted and equal but oppositely directed magnetic currents are placed on the two sides of the short as shown in Fig. 3. Two equivalent models are then formed as suggested in Fig. 4. The current on the PEC C_S is imaged, leaving equivalent current J_z on C_S and the image of J_z in the region $y > 0$, as depicted in Fig. 4a. C_S and the surface on which the image of J_z resides together constitute a surface designated C_S^i. The tangential component of the total electric field is forced to be zero on C_S^i while equality of tangential magnetic field is enforced as the shorted aperture is approached from either side in the two equivalent models. These equations are then solved numerically to determine the magnetic current on the short as well as the equivalent electric current on C_S^i , which are in turn used to compute the total fields in the original problem. These methods remain valid for cases in which the interior and exterior materials are different.

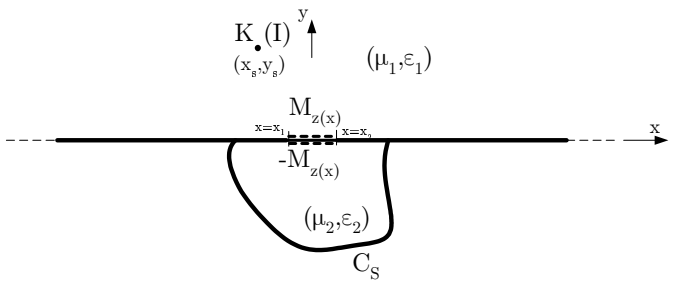

Figure 3: Structure for TE (TM) coupled integral equations with shorted aperture

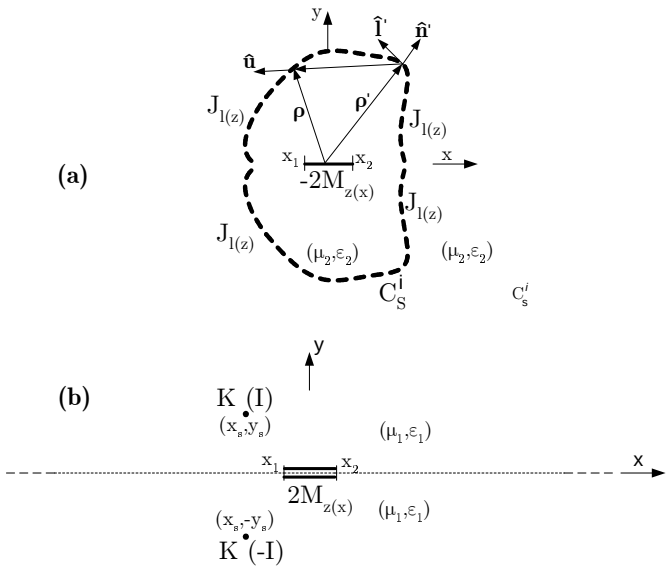

Figure 4: Equivalent models for TE (TM) coupled integral equations method: (a) - Interior equivalent model; (b) - Exterior equivalent model

3.2.1 Coupled Integral Equations (TE)

If the following Green's function is defined,

$$G^A\left(x,y;x',y';k,Z\right) = -\frac{k}{4Z}H_0^{(2)}\left(kR\right) \tag{19}$$

with $R = \sqrt{\left(x-x'\right)^2+\left(y-y'\right)^2}$, then the tangential magnetic field at the aperture in the exterior-region model is given by

$$H_z^o\left(x,0\right) = H_z^{s.c.}\left(x,0\right) + \mathcal{H}_z^o\left[2M_z;x,0\right] \tag{20}$$

where

$$\mathcal{H}_z^o\left[M_z;x,0\right] = \int_{x_1}^{x_2} M_z\left(x'\right) G^A\left(x,0;x',0;k_1,Z_1\right) dx' \tag{21}$$

with

$$H_z^{s.c.}(x,0) = 2e^{jk_1 x\cos\phi_0} \tag{22}$$

for plane wave excitation and

$$H_z^{s.c.}(x,0) = 2KG^A(x,0;x_s,y_s;k_1,Z_1) \tag{23}$$

for the case of a line source of strength K. $H_z^{s.c.}(x,0)$ is the z component of the incident magnetic field that exists at the short-circuited aperture. Subject to the following Green's function definition

$$G^B(x,y;x',y';k) = -\frac{k}{4j}\cos(\theta')\,H_1^{(2)}(kR) \tag{24}$$

where

$$\cos\theta' = \hat{\mathbf{u}}\cdot\hat{\mathbf{n}}' \quad , \quad \hat{\mathbf{u}} = \frac{\rho-\rho'}{|\rho-\rho'|} \quad , \quad \hat{\mathbf{n}}' = \hat{\boldsymbol{\ell}}'\times\hat{\mathbf{z}} \tag{25}$$

(see Fig. 4), where the total z-directed magnetic field in the interior-region model is given by

$$H_z^i(x,y) = \mathcal{H}_z^i[-2M_z;x,y] + \mathcal{H}_z^i[J_l;x,y] \tag{26}$$

where

$$\mathcal{H}_z^i[M_z;x,y] = \int_{x_1}^{x_2} M_z(x')\,G^A(x,y;x',0;k_2,Z_2)\,dx' \tag{27}$$

and where

$$\mathcal{H}_z^i[J_l;x,y] = \int_{C_s^i} J_l(x',y')\,G^B(x,y;x',y';k_2)\,dl'. \tag{28}$$

The coupled integral equations are

$$H_z^o(x,0) - H_z^i(x,0) = -H_z^{s.c.}(x)\ ,\ x \in (x_1, x_2)\,, \tag{29}$$

which enforces continuity of the z component of magnetic field in the aperture, and

$$H_z^i(x,y) - \frac{J_l(x,y)}{2} = 0\ ,\ x,y \in C_S^i, \tag{30}$$

which enforces the requirement that the component of the electric field tangential to and on C_S^i be zero. Specifically, the tangential component of the electric field is zero on C_S^i in Fig. 4, which means that outside C_S^i the field is zero. In particular, then, the component of the magnetic field tangential to and on the exterior side of C_S^i is zero, causing its value on the interior side to be $\hat{\mathbf{n}} \times \left(J_l \hat{\boldsymbol{\ell}}\right)$, as implied by (30). The condition that the x component of electric field be zero on the x-z plane is enforced in both models through the use of image theory embodied in the equations. The equivalent electric and magnetic currents are expanded in piecewise-linear and rectangular pulses, respectively, equation (29) is point matched, and equation (30) is tested with rectangular pulses to obtain a matrix form of the coupled integral equations.

3.2.2 Coupled Integral Equations (TM)

The x-directed electric vector potential associated with the magnetic current across the short must be a solution to the wave equation

$$\left(\nabla_{xy}^2 + k^2\right) F_x = -\varepsilon K l \delta(x - x')\,\delta(y - y')\,. \tag{31}$$

Subject to the jump condition on E_z , the solution to (31) is determined to be

$$F_x\left(x,y;x',y';k\right)=\frac{\varepsilon Kl}{4j}H_0^{(2)}\left(kR\right). \tag{32}$$

The x-directed component of the corresponding magnetic field and the z-directed component of the electric field can be determined from (32) and are employed in the formulation of the coupled integral equations. Similar field components due to the equivalent electric current on C_s^i are determined from the magnetic vector potential

$$A_z\left(x,y;x',y';k\right)=\frac{\mu I}{4j}H_0^{(2)}\left(kR\right). \tag{33}$$

The coupled integral equations are formed with the magnetic current on the short and the equivalent electric current on C_s^i as the unknowns. The tangential component of the magnetic fields in the two regions is forced to be equal by

$$H_x^M\left[2M_x\left(x'\right);k_1;x,0\right]-H_x^M\left[-2M_x\left(x'\right);k_2;x,0\right]-$$

$$H_x^J\left[J_z\left(x',y'\right);k_2;x,0\right]=-H_x^{s.c.}(x,0),\ \ x\in(x_1,x_2) \tag{34}$$

in the limit as the aperture is approached from either side, where

$$H_x^M\left[M_x\left(x'\right);k;x,0\right]=-\frac{1}{4kZ}\left[\left(k^2+\frac{\partial^2}{\partial x^2}\right)\int_{x_1}^{x_2}M_x(x')H_0^{(2)}\left(k\left|x-x'\right|\right)dx'\right], \tag{35}$$

$$H_x^J\left[J_z\left(x',y'\right);k;x,0\right]=-\frac{k}{4j}\int\limits_{C_S^i}J_z\left(x',y'\right)\frac{(y-y')}{R}H_1^{(2)}\left(kR\right)dl'\ ,\ x\in(x_1,x_2), \tag{36}$$

and where

$$H_x^{s.c.}\left(x,0\right)=e^{jk_1x\cos\phi_0}+e^{jk_1x\cos\left(\frac{3\pi}{2}-\phi_0\right)} \tag{37}$$

for plane wave excitation and

$$H_x^{s.c.}\left(x,0\right)=\frac{Ik_1}{2j}\frac{y_s}{R_s}H_1^{(2)}\left(k_1R_s\right) \tag{38}$$

with $R_s = \sqrt{(x-x_s)^2 + y_s^2}$ for line source excitation. The variable l' in (36) is defined as the arc displacement along the contour C_S^i , and allows one to express the source coordinates as functions of l' : $y' = y'(l')\,;\, x' = x'(l')$. The tangential component of electric field is constrained to be zero on C_S^i by

$$E_z^M\left[-2M_x\left(x'\right);k_2;x,y\right] + E_z^J\left[J_z\left(x',y'\right);k_2;x,y\right] = 0 \quad x,y \in C_S^i \tag{39}$$

where

$$E_z^M\left[M_x\left(x'\right);k;x,y\right] = \frac{jk}{4}\int_{x_2}^{x_1} M_x\left(x'\right)\frac{y}{\sqrt{(x-x')^2+y^2}}H_1^{(2)}\left(k\sqrt{(x-x')^2+y^2}\right)dx' \tag{40}$$

and

$$E_z^J\left[J_z\left(x',y'\right);k;x,y\right] = -\frac{kZ}{4}\int_{C_S^i} J_z\left(x',y'\right)H_0^{(2)}\left(kR\right)dl'. \tag{41}$$

The equivalent electric and magnetic currents are expanded in rectangular and piecewise-linear pulses, respectively, equation (39) is point matched and equation (34) is tested with rectangular pulses to obtain a matrix form of the coupled integral equations.

4 Numerical results

This section is devoted to the comparison of numerical results obtained by evaluating the analytical formulas of [1] with those obtained by the integral equation methods developed in Section 3. The comparisons are presented in two forms: linear plots of $|E_z|$ or $|H_z|$ along the y axis and contour plots of $|E_z|$ or $|H_z|$ inside and near the cavity. The y axis is chosen for the linear plots because the transition from the interior

to the exterior of the cavity is easily observed along this line. The advantage of the linear plots is that multiple curves can be presented in the same graph, which allows one to analyze variations in the fields with respect to various parameters such as the type of material in the cavity or the frequency of the source. In contrast, the contour plots provide a more complete depiction of field behavior but are not amenable to displaying multiple cases in a single graph.

In all the results that follow, the semielliptical cavity corresponds to $\xi_1 = 2$. For the linear plots, Figs. 5 and 8 contain three graphs corresponding to three cases for the media in the two regions: $\zeta = 1$, $\zeta = 1/2$, $\zeta = 2$, where $\zeta = Z_1/Z_2$. Each graph displays the total field on the y axis for three different values of the dimensionless quantity c of (13): $c = 0.1, \pi, 4.5$. No noticeable difference occurs between the results obtained from the exact solutions of [1] and those obtained from numerical solutions of the integral equations.

For the contour plots, the fields are computed at the nodes of a rectangular grid of 181×362 points along the horizontal and vertical directions, respectively. The computation time is in the order of a few minutes on a Windows PC with clock speed of 1.5GHz.

The evaluation of the analytic expressions of [1] becomes quite difficult for some combinations of the parameters when line sources are present. In particular, numerical convergence issues are resolved by using the acceleration technique described in [4]. Further details on the computations of the Mathieu functions are provided in the Appendix.

The finite ground plane methods of Section 3 are only valid in special cases where the source is TM-polarized and the materials in both regions are the same, and hence data from these methods are only presented in these cases. In these calculations, the finite ground plane was set to a total width of $7d$, which provides very accurate results for the source and observation points of the cases considered.

4.1 Plane wave excitation

TM polarization. Plots of the total z-directed electric field along the y-axis are presented in Fig. 5 for the case where a unit amplitude plane wave is incident at an angle $\varphi_0 = 45°$. In this figure, the results obtained from the evaluation of the analytical formulas (11-13) of [1] are overlapped with those obtained from the IE methods of Section 3. Specifically, the scatterer method of Section 3.1.1 is applied to obtain the data shown in Fig. 5a, while the data of Figs. 5b,c are obtained by application of the coupled integral equation method of Section 3.2.2.

One observes that changing ζ does not vary the fields significantly and that for the considered cases the field well inside the cavity is largest when $c = \pi$, which corresponds to $\lambda = d$, *i.e.*, the wavelength is equal to the aperture width.

4.2 Line source outside cavity

For both polarizations, the line source is located in region 1 at coordinates ($\xi_0 = 1.5, v_0 = 30°$). The strength of the line source is adjusted so that the z-directed component of the incident field is expressed as a zero-order Hankel function of the

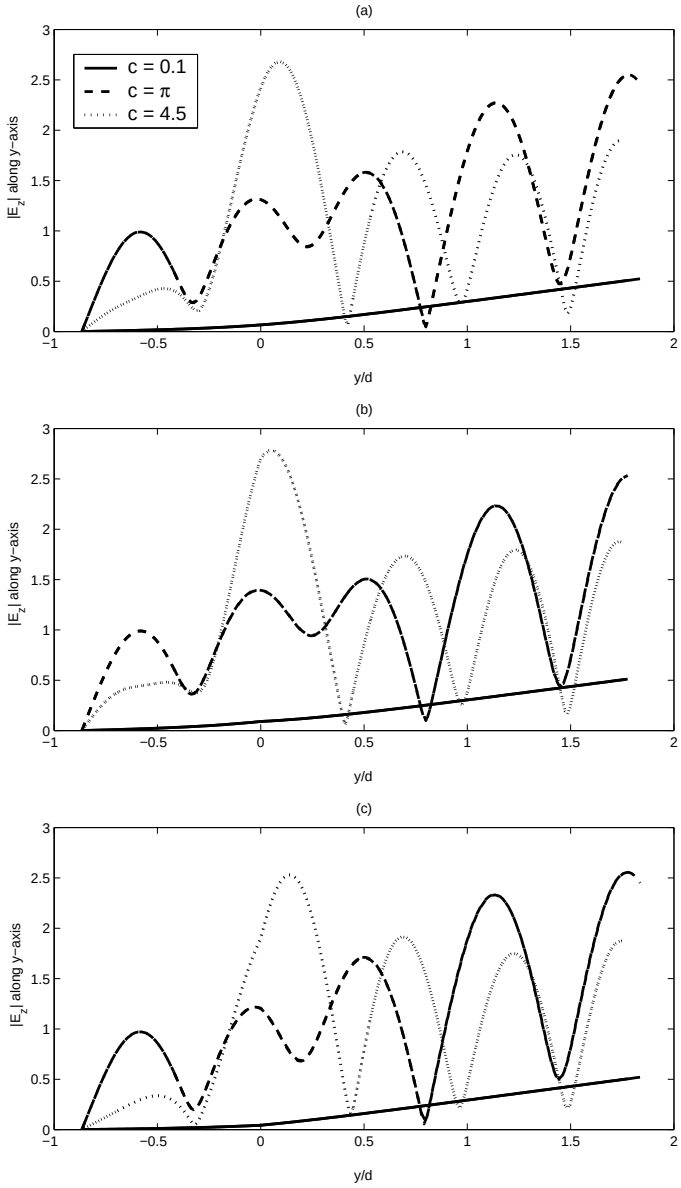

Figure 5: $|E_z|$ for a TM polarized plane wave incident at $\varphi_0 = 45°$. (a) $\zeta = 1$; (b) $\zeta = 1/2$; (c) $\zeta = 2$.

second kind with no weighting coefficient.

4.2.1 TM polarization

A contour plot of $|E_Z|$ for the case where $c = 0.1$ and $\zeta = 1/2$ is shown in Fig. 6. The total field is computed by evaluation of analytical expressions (44-46) of [1] and also by application of the coupled integral equation method of Section 3.2.2. Fig. 7 displays a contour plot of the magnitude of the difference between the data obtained from these two methods.

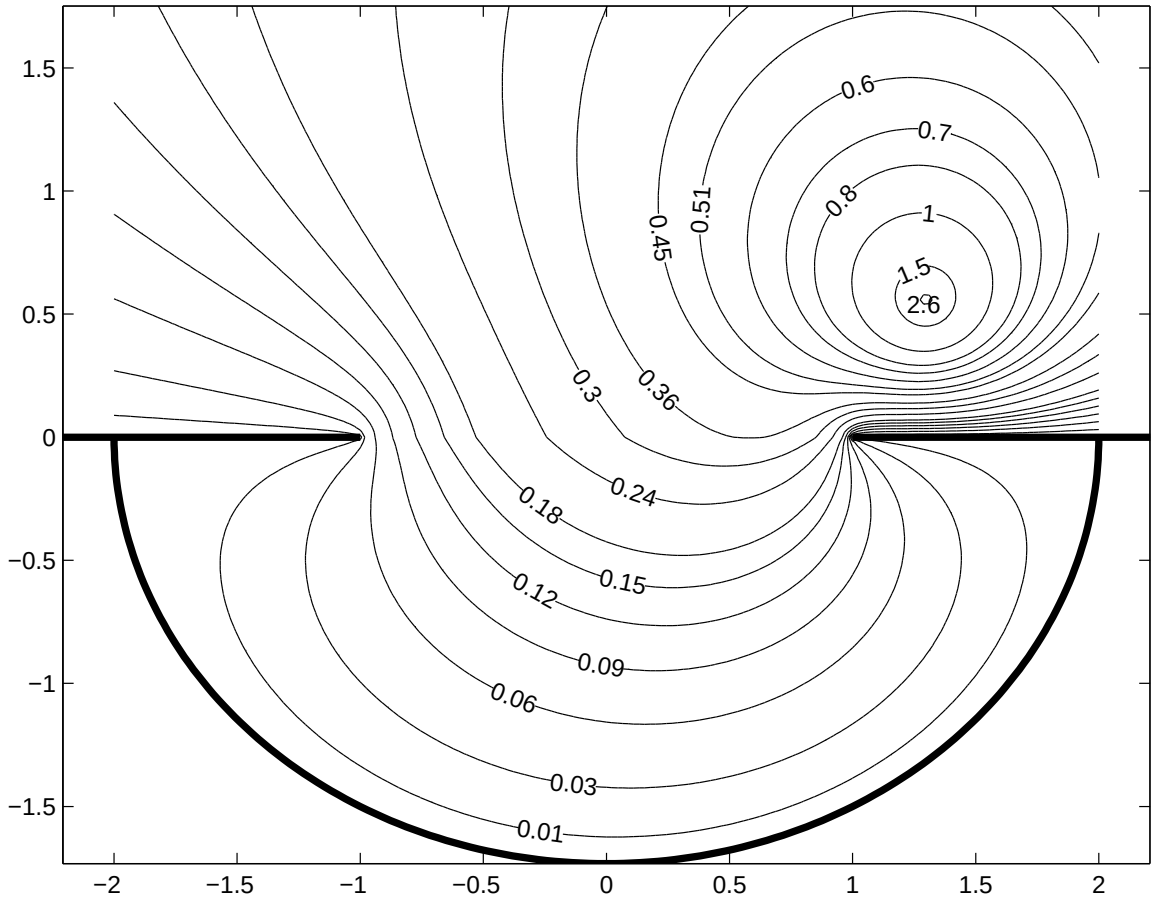

Figure 6: Contour plot of $|E_z|$ for an electric line source located at $(\xi_0 = 1.5, v_0 = 30^\circ)$ when $c = 0.1$ and $\zeta = 1/2$.

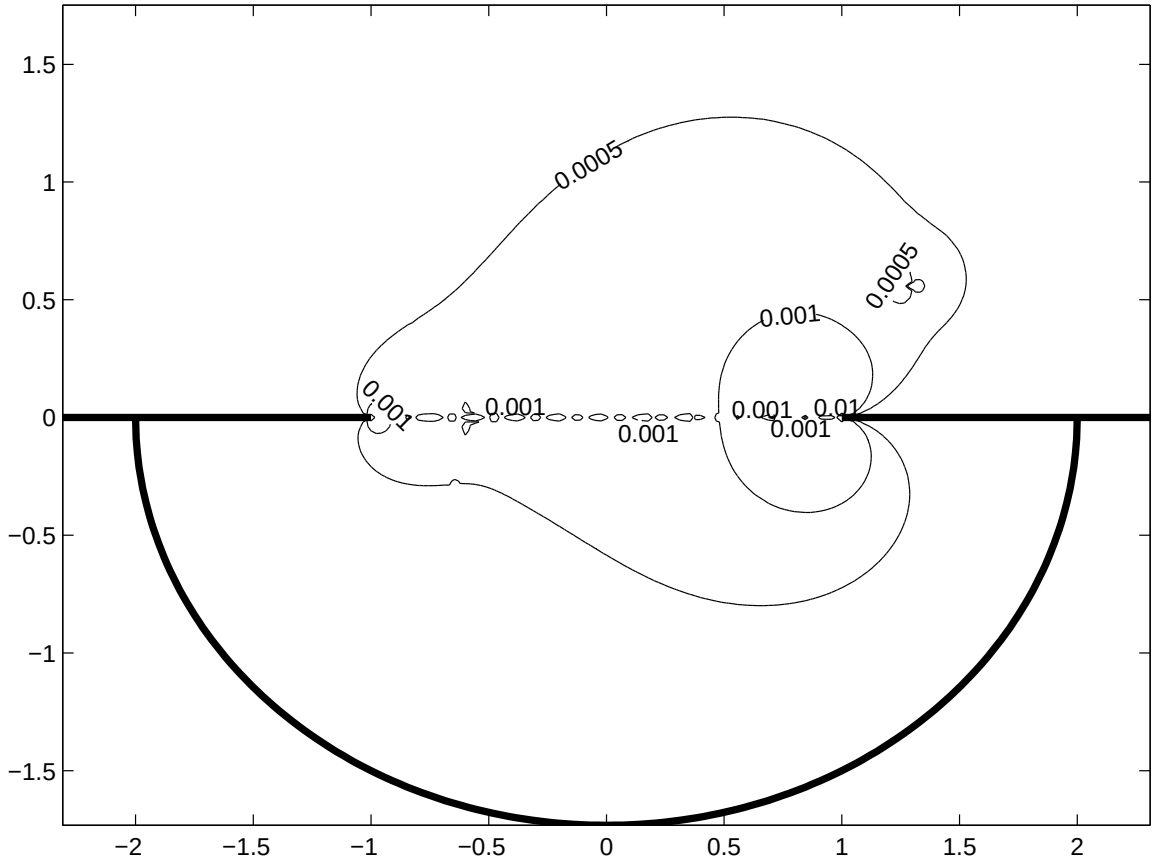

Figure 7: Contour plot of $|E_z^{I.E.} - E_z^{analytic}|$ for the results shown in Fig. 6.

4.2.2 TE polarization

The total magnetic field for the case of a magnetic line source located outside the cavity is presented in Fig. 8. Data obtained from evaluation of (63-64) of [1] are plotted along with those from the IE method of Section 3.2.1. One observes that a change in ζ does not vary the qualitative behavior of the three curves and that the strongest field inside the cavity is achieved when $c = 0.1$.

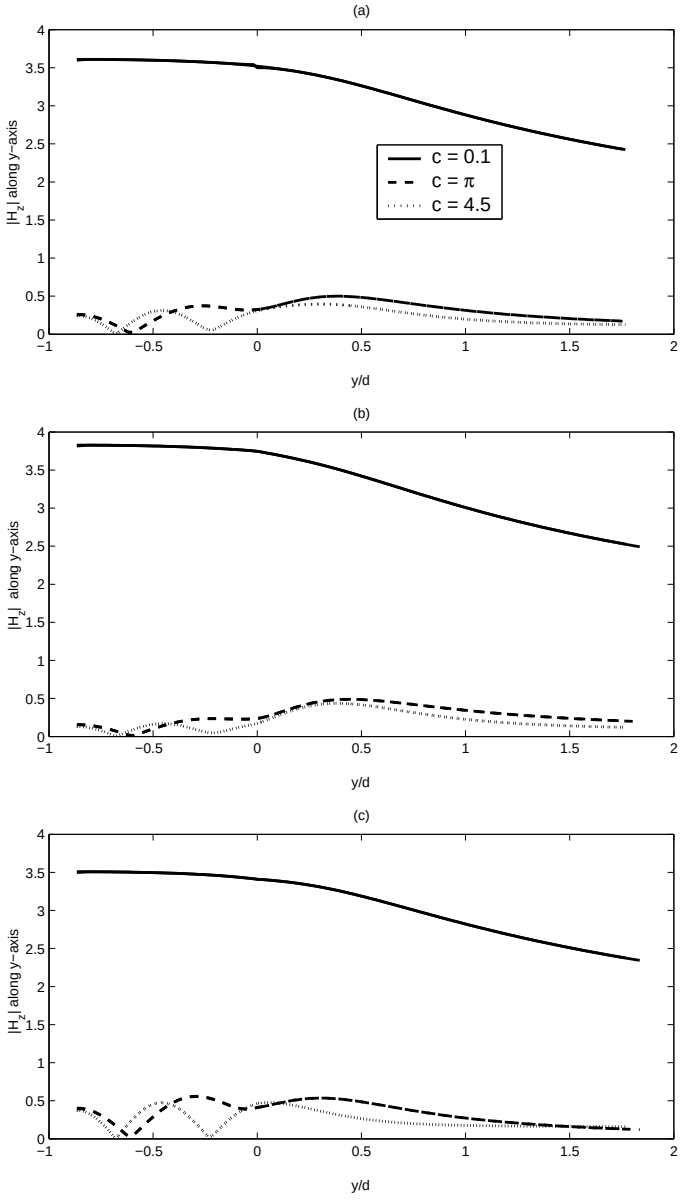

Figure 8: Magnetic line source located outside the cavity at $\xi_0 = 1.5$ and $v_0 = 30°$. (a) $\zeta = 1$; (b) $\zeta = 1/2$; (c) $\zeta = 2$.

4.3 Line source inside cavity

TE polarization A line source is located inside the cavity (region 2) at coordinates $(\xi_0 = 1.5, v_0 = -75°)$. The strength of the line source is adjusted so that the z-

directed component of the incident field is expressed as a zero-order Hankel function of the second kind with no weighting coefficient. Fig. 9 displays the contour plot of $|H_z|$ for the case where $c = \pi$ and $\zeta = 1/2$. These data are obtained by evaluation of (69-70) of [1] and also by application of the IE method of Section 3.2.1. Fig. 10 displays the magnitude of the difference in the data obtained from the two approaches.

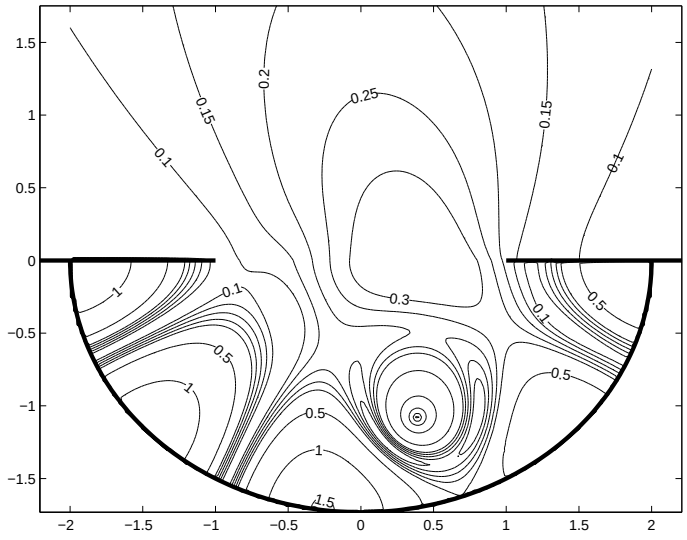

Figure 9: Contour plot of $|H_z|$ for a magnetic line source located at $(\xi_0 = 1.5, v_0 = -75^\circ)$ when $c = \pi$ and $\zeta = 1/2$.

4.4 Reciprocity

The results obtained from the integral equations were shown to satisfy reciprocity. The source and observation points were interchanged for a number of cases and the computed fields were shown to adhere to reciprocity. By inspection, one notes that the analytical expressions for the fields are consistent with reciprocity.

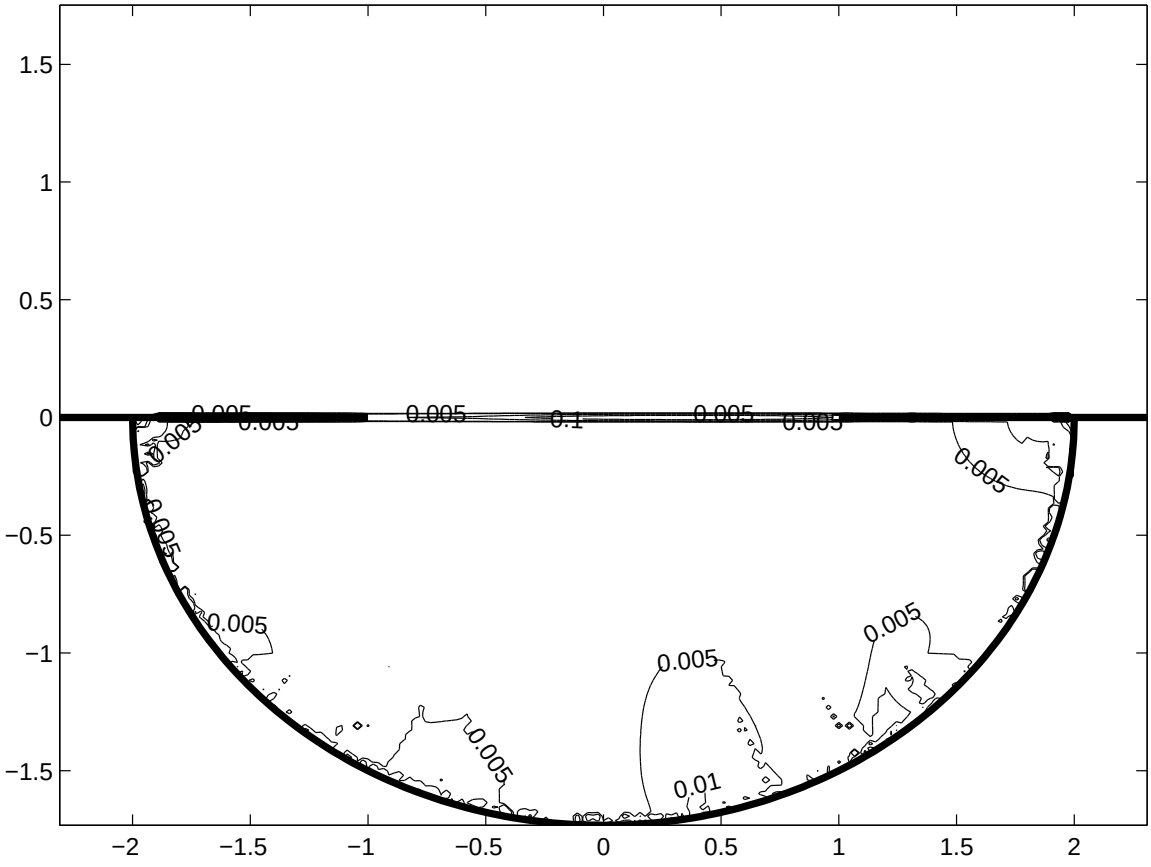

Figure 10: Contour plot of $|H_z^{\text{I.E.}} - H_z^{\text{analytic}}|$ for the results shown in Fig. 9. No contour lines are shown for $y > 0$ because the differences are negligible.

5 Conclusion

Three independent integral equations were utilized to investigate the structure of Fig. 1 and numerical results were compared with those obtained from the evaluations of the analytical formulas derived in [1]. The numerical results of Section 4 show excellent agreement between the canonical solutions in [1] and the integral equation methods for all cases of excitation and isorefractive materials considered. The mutual validation of these two approaches to determine the fields present in the structure of

Fig. 1 provides a good validation test for computer codes, involving a cavity, different materials, and sharp edges.

A Computation of Mathieu functions

The evaluation of the analytical formulas requires the computation of Mathieu functions. The calculations for this work were performed with FORTRAN subroutines reported in [5]. These subroutines compute Mathieu functions according to the Goldstein-Ince normalization [6],[7] and, therefore, had to be modified to compute them according to Stratton's normalization which corresponds to the notation used in [1]. The subroutines of [5] compute two sets of Mathieu functions. The first set represents the solutions of the equation

$$\frac{d^2y}{dz^2} + (\lambda - 2q\cos 2z)y = 0, \tag{42}$$

which are usually called Mathieu functions and, apart from the normalization, correspond to Stratton's angular functions. The second set is given by the solutions of

$$\frac{d^2y}{dz^2} - (\lambda - 2q\cosh 2z)y = 0, \tag{43}$$

which are called modified Mathieu functions and correspond to Stratton's radial functions, again, apart from a normalization. Stratton's version of (42) is written as

$$\frac{d^2f_2}{dv^2} + (b - c_0^2\lambda_0^2\cos^2 v)f_2 = 0 \tag{44}$$

where b is the separation constant, c_0 is half the focal distance, and λ is the wavevector. Therefore, the parameter q in (42) is related to the product $c_0\lambda_0$ in (44) and to the

dimensionless parameter c of (13) by

$$q = \frac{1}{4}c_0^2\lambda_0^2 = \frac{1}{4}c^2. \tag{45}$$

The theory of Mathieu functions that is necessary to understand the analytical formulation used in this work is found in [8], whereas a clear explanation of the practical computation of Mathieu functions is given in [9] and [10]. These last two references are of great help in clarifying the different notations and normalizations introduced by different authors who have studied Mathieu functions. A good collection of information on Mathieu functions is found in [11] and further references are given in [12].

References

[1] P.L.E. Uslenghi, "Exact penetration, radiation and scattering for a slotted semielliptical channel filled with isorefractive material," *IEEE Trans. Antennas Propagat.*, to appear in the June 2004 issue.

[2] J.D. Shumpert and C.M. Butler, "Penetration through slots in conducting cylinders: Part 1, te case, analysis of a strip in a waveguide," *IEEE Trans. Antennas Propagat.*, vol. 46, no. 11, pp. 1612–1621, November 1998.

[3] C.M. Butler, "Investigation of a scatterer coupled to an aperture in a conducting screen," *Proc. IEE (London)*, vol. 127, Pt. H, no. 3, pp. 161–169, June 1980.

[4] D. Erricolo, "Acceleration of the convergence of series containing Mathieu functions using Shanks transformation," *IEEE Antennas and Wireless Propagation Letters*, vol. 2, pp. 58–61, 2003.

[5] S. Zhang and J. M. Jin, *Computation of Special Functions*, Wiley, New York, 1996.

[6] S. Goldstein, "Mathieu functions," *Camb. Phil. Soc. Trans.*, vol. 23, pp. 303–336, 1927.

[7] E. L. Ince, "Tables of elliptic cylinder functions," *Roy. Soc. Edin. Proc.*, vol. 52, pp. 355–423, 1932.

[8] J. A. Stratton, *Electromagnetic Theory*, McGraw-Hill, New York, 1941.

[9] National Bureau of Standards, *Tables relating to Mathieu Functions*, Columbia University Press, New York, 1951.

[10] G. Blanch and I. Rhodes, "Tables of characteristic values of mathieu's equation for large values of the parameter," *J. Washington Academy of Sciences*, vol. 45, no. 6, pp. 166–196, June 1955.

[11] F. P. Mechel, *Mathieu functions: formulas, generation, use*, S. Hirzel Verlag, 1997.

[12] M. Abramovitz and I. A. Stegun, *Handbook of Mathematical Functions*, Dover Publications, Inc, New York, 1970.